Imaging of Oxygen Diffusion in Individual Pt/$Ce_2Zr_2O_x$ Catalyst Particles for Oxygen Storage/Release Cycle**

Hirosuke Matsui*, Nozomu Ishiguro, Kaori Enomoto, Oki Sekizawa, Tomoya Uruga, and Mizuki Tada*

Abstract: The spatial distribution of Ce^{3+} and Ce^{4+} in each particle of $Ce_2Zr_2O_x$ in a three-way conversion catalyst system was successfully imaged for oxygen storage/release cycle by scanning X-ray absorption fine structure (XAFS) using hard X-ray nanobeams. The nano-XAFS imaging visualized and identified the modes of heterogeneous oxygen diffusion from the interface of Pt catalyst and $Ce_2Zr_2O_x$ support and active parts in individual catalyst particles for the first time.

Heterogeneous solid catalysts are utilized for various chemical processes and intrinsically consist of structural inhomogeneity. The most typical form of solid catalysts is powder, which is an assembly of inhomogeneous particles with different structural components (morphology, surface structure, domain boundary, oxygen content, etc.).[1] In practice, the reactivity of a solid catalyst is evaluated based on the average of these structural components, and as a result, it remains difficult to understand the real variation of the active parts in a heterogeneous catalyst. To solve this problem, spatially-resolved imaging of chemical states in an individual catalyst particle is highly demanded to reveal active parts and heterogeneous reaction modes in nanoscale.

Ce is the key element for the oxygen storage/release function in an automobile exhausting-gas cleaning three-way catalyst system, and a redox process between Ce^{3+} and Ce^{4+} controls oxygen content in these catalyst systems.[2] However, it is well known that only Ce species with extensive surface defects can contribute to the redox process in pure ceria that offers insufficient oxygen storage/release capacity. $Ce_2Zr_2O_x$ (CZ; x = 7–8) solid-solution crystal has been reported to have the ordered arrangement of Ce and Zr and exhibit excellent oxygen storage/release properties.[3] Almost 90% of the Ce atoms in CZ bulk can participate in the redox process between oxidized κ-phase $Ce_2Zr_2O_8$ and reduced pyrochlore $Ce_2Zr_2O_7$. Stoichiometric changes in the Ce valence states with oxygen diffusion in CZ bulk offers remarkable catalytic performance such as in automobile exhaust-gas cleaning on Pt/CZ[4, 5] and methane steam-reforming on Ni/CZ[6].

Recently, there have been remarkable developments in X-ray imaging techniques[7] and XAFS imaging is promising for revealing heterogeneous behavior in practical materials.[8] We previously reported the spatial distribution of Ce oxidation states in individual particles of Pt/CZ catalysts by spatially-resolved scanning nano-XAFS.[9] The *ex-situ* nano-XAFS analysis revealed differences in Ce oxidation states in individual Pt/CZ particles with different oxygen contents. However, the size of Pt nanoparticles on CZ surfaces (< 10 nm) was much smaller than the size of probe X-ray beams (> 100 nm), and it was not reported the detail of oxygen diffusion from the interface of the Pt catalyst into CZ bulk because of the lack of spatial information about the Pt nanoparticles on CZ support.

In this paper, we report the imaging of oxygen diffusion in individual CZ particles in contact with micron-sized catalytically active Pt particle for a reversible oxygen storage/release cycle. We investigated the nano-XAFS imaging with 100 nm-sized hard X-ray beams for several CZ particles with different locations of attached Pt particles and the two-dimensional images of Ce oxidation states, which showed the mode of oxygen diffusion, were recorded during oxygen storage/release processes. The present study clearly revealed how Ce valence states in the CZ particles changed from the interface of the Pt catalyst via oxygen diffusion for the first time.

Micron-sized Pt particles (Alfa Aesar, 0.2–1.6 μm) and CZ particles (0.2–2.0 μm) were dispersed on a SiN membrane by an impregnation method. SEM analysis measured by BEI mode

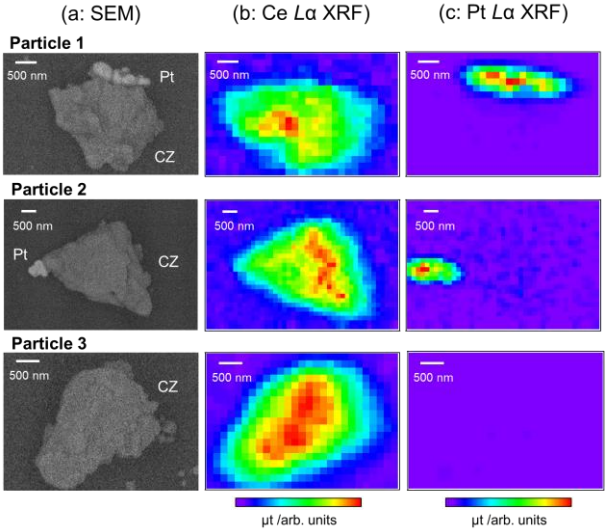

Figure 1. (A) SEM images (BEI mode), (B) Ce *L*α, and (C) Pt *L*α XRF mappings of three CZ particles (**1**–**3**) on a SiN membrane.

[*] Dr. H. Matsui, Ms. K. Enomoto, Prof. Dr. M. Tada
Department of Chemistry, Graduate School of Science &
Research Center for Materials Science (RCMS) &
Integrated Research Consortium on Chemical Sciences (IRCCS),
Nagoya University
Furo, Chikusa, Nagoya, Aichi 464-8602 (Japan)
E-mail: mtada@chem.nagoya-u.ac.jp
Dr. N. Ishiguro, Prof. Dr. M. Tada
RIKEN SPring-8 Center
Koto, Sayo, Hyogo 679-5198 (Japan)
Dr. O. Sekizawa, Prof. Dr. T. Uruga
Innovation Research Center for Fuel Cells,
The University of Electro-Communications
Chofu, Tokyo 182-8585 (Japan)
Prof. Dr. T. Uruga
Japan Synchrotron Radiation Research Center, SPring-8
Koto, Sayo, Hyogo 679-5198 (Japan)

[**] The authors thank Dr Y. Nagai (Toyota Central R&D Labs. Inc.). We also thank Dr. S. Nakao (IMS) for SEM measurements and Ms. N. Takada (IMS) for sample preparation. XAFS measurements were performed with the approval of SPring-8 proposals (2011B1889, 2013B7821, 2014A7821, 2014B7821, and 2015A7821). This work was supported in part by the NEXT program (GR090), the NEDO program, Grant-in-Aid for Scientific Research KAKENHI Kiban B (26288005), Grant-in-Aid for Young Scientists B (16K18288), and the Murata Science Foundation.

Supporting information for this article is given via a link at the end of the document.

showed significant contrast between Pt (bright image) and CZ particles (dark image) (Figs. 1(a) and S1). We selected several isolated CZ particles with different Pt locations on the SiN membrane: (**Particle 1**) a CZ particle with Pt attached to the side of the particle, (**Particle 2**) a CZ particle with Pt attached to the edge corner of the particle, and (**Particle 3**) a CZ particle without Pt (Figs. 1(a) and S2). Ce *L*α and Pt *L*α XRF mappings using nano X-ray beams clearly showed the locations and morphologies of both Pt and CZ particles in the selected assemblies as shown in Figs. 1(b) and 1(c).

CZ and Pt/CZ exhibited sufficient oxygen storage/release performances: 86% of stoichiometric oxygen was contributed by temperature-programmed reduction and oxidation (TPR and TPO) (Fig. S3). It was found that the attachment of Pt significantly changed the temperature of oxygen release by reduction, while the temperature of oxygen storage was not affected by the attachment of Pt. At 573 K, the phase transition between κ-phase $Ce_2Zr_2O_8$ and pyrochlore $Ce_2Zr_2O_7$ completed reversibly, as characterized by X-ray diffraction and Raman spectra. When $Ce_2Zr_2O_8$ was reduced to $Ce_2Zr_2O_7$ at 573 K, the (440) diffraction peak shifted from 48.8 to 47.7 deg.; the Raman peaks attributed to Zr-O bonds in $Ce_2Zr_2O_8$[10] changed to the broad peaks of $Ce_2Zr_2O_7$[11] (Fig. S4).

We measured X-ray diffraction of CZ particles dispersed on the SiN membrane and investigated the variation of oxygen storage/release reactivity in these CZ particles on the membrane. The (440) peak at 48.8 deg. in a fully-oxidized sample (Fig. S5(1)) shifted to around 48.0 deg. and significantly broadened by the reduction at 423 K (Fig. S5(2)), indicating that most of the supported CZ particles had reacted but there was significant variation in the local reactivity at this reaction temperature. A similar shift in the (440) diffraction peak was also observed in the oxygen storage process at 423 K (Fig. S5(4)), while broadening of the peak was relatively small compared to the oxygen release process. Further reduction and oxidation at 573 K completed both oxygen release and storage, resulting in the formation of the sharp peaks of pyrochlore $Ce_2Zr_2O_7$ and κ-phase $Ce_2Zr_2O_8$, respectively (Figs. S5(3) and S5(5)). These results suggest that the supported CZ particles macroscopically followed the reversible oxygen storage/release behavior under the identical reaction conditions. However, there were significant differences in the reactivity of the oxygen storage/release on each CZ particle, and the reactions at 423 K would show intermediate phases and mode of oxygen diffusion for the oxygen storage/release inside the CZ particles.

Hence, we investigated the nano-XAFS analysis of the three CZ particles for the oxygen storage/release processes at 423 and 573 K. Scanning nano-XAFS spectra were measured at the BL36XU and BL39XU undulator beamlines at SPring-8 (Fig. S6). Monochromatized X-rays around 6 keV were focused by Kirkpatrick-Baez mirrors to a size of 409 (h) × 154 (v) nm to irradiate a sample enclosed in a XAFS cell mounted on an encoded-feedback translation stage. Two-dimensional nano-X ray fluorescent images of the sample were obtained with a step size of 150 nm in the energy range of the Ce L_{III}-edge (Fig. S7), for which the XANES spectrum is highly sensitive to valence changes between Ce^{3+} and Ce^{4+}. The ratio of peak intensities at 5.7302 keV (assigned to the $2p \rightarrow 4f^1 5d^1$ (B_0) mode transition of Ce^{3+}) and 5.7344 and 5.7410 keV (assigned to the $2p \rightarrow 4f^1 5d^1 L$ (B_1) mode and $4f^0 5d^1$ (C) mode transitions of Ce^{4+}) is relative to the Ce valence states between Ce^{3+} and Ce^{4+} (Fig. S8).[12] Although three-dimensional structural information is reduced to two-dimensional projection by nano-XAFS, the intensity ratio of these peaks provided the two-dimensional mapping of Ce^{3+}/Ce^{4+} distribution in each particle for the oxygen storage/release as shown in Fig. 2.[9]

In the case of **Particle 1** in which the Pt was attached to the side of the CZ particle, the Ce valence state changed smoothly during both oxygen storage and release processes at 573 K (Figs. 2(b-1) and 2(d-1)). The heterogeneous distribution

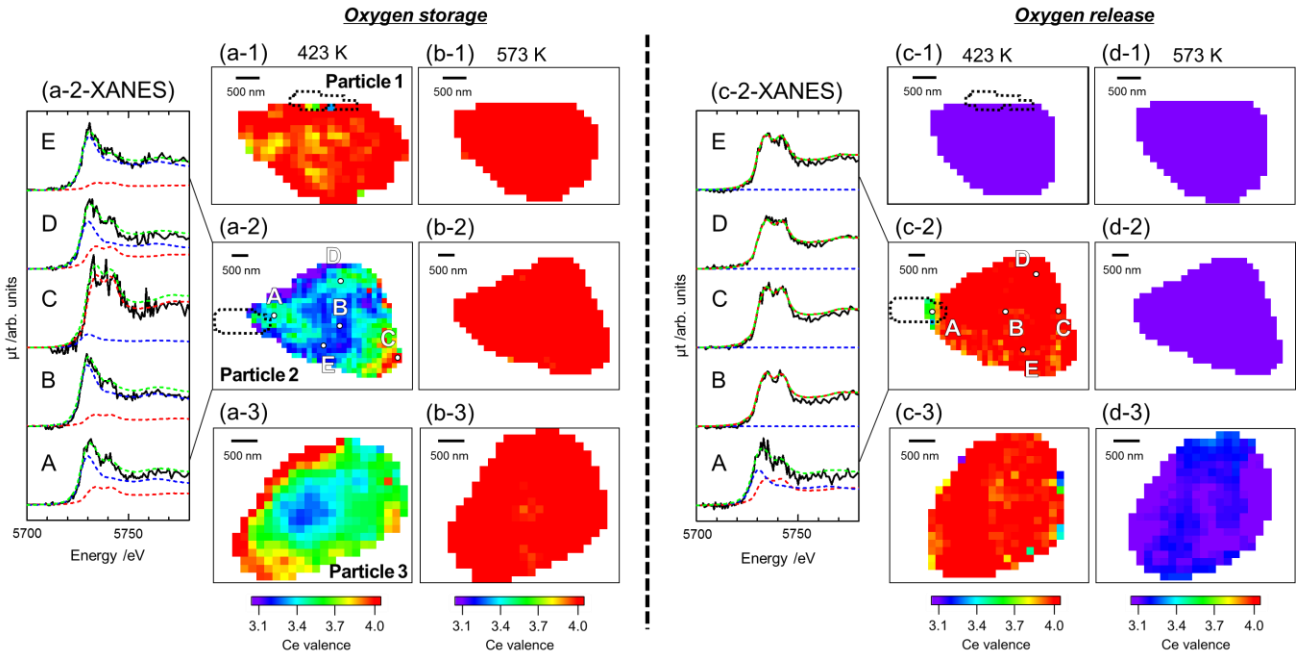

Figure 2. (a-d) The 2D mappings of Ce valence states of **Particles 1–3** after the oxygen storage and release processes at 423 and 573 K. Black dotted lines indicate the position of Pt particles. (a/c-2-XANES) Ce L_{III}-edge nano-XANES spectra (black lines) were shown at the representative points of **A–E** in **Particle 2**. Blue, red, and green dash lines present fitted spectra of Ce^{3+}, Ce^{4+}, and their summation. Oxygen storage and release were processed with flow of O_2 or 10% H_2/N_2 in 1000 mL min^{-1} for 1 h.

of unreacted parts inside the CZ particle was observed by the oxygen storage at 423 K, but it was irrelevant to the position where the Pt catalyst was attached (Fig. 2(a-1)). Such heterogeneous distribution of unreacted parts was not observed in the oxygen release process at 423 K on **Particle 1** (Fig 2(c-1)).

It should be noted that **Particle 2** in which the Pt particle was attached to the edge corner of the CZ particle exhibited an isotropic gradient in the oxidation state of Ce^{3+} an Ce^{4+} with the center of Pt particle, suggesting that Pt catalyst played a crucial role in the oxygen release. For oxygen storage at 423 K, a significant contrast colored in purple–red was observed across the entire area of the CZ particle (Fig. 2(a-2)). This was observed to be independent of the position of the attached Pt, indicating that oxygen storage occurred in domains of the CZ particle without the contribution of the Pt catalyst. We performed the deconvolution of the Ce L_{III}-edge nano-XANES spectra at the representative positions **A–E** in **Particle 2** to the XANES spectra of pyrochlore $Ce_2Zr_2O_7$ (Ce^{3+}; blue dash line) and κ-phase $Ce_2Zr_2O_8$ (Ce^{4+}; red dash line) presented in Fig. 2(a-2-XANES). The nano-XANES spectra at positions **A–E** were significantly different, reflecting the variations in the valence states of Ce species, and agreed with the 2D mapping of the Ce oxidation states in Fig. 2(a-2). After oxidation at 573 K, all Ce species in **Particle 2** were fully converted to Ce^{4+} (Fig. 2(b-2)).

In contrast, it was found that oxygen release was remarkably controlled by the Pt catalyst. The oxygen release at 423 K started from the area where the Pt was attached as shown in Fig. 2(c-2). The Ce L_{III}-edge nano-XANES spectra suggest that 50% of the Ce at position **A** close to the Pt catalyst was converted to Ce^{3+}, while positions **B–E** far from the Pt catalyst did not react at all at this stage (Fig. 2(c-2-XANES)). These results clearly suggest that the initiation of oxygen release locally proceeds from the attached Pt catalyst and oxygen diffusion spreads into the CZ bulk. The scanning nano-XAFS imaging evidenced the significance of the interface between the Pt catalyst and the CZ particle as a preferential oxygen release site though the detail of the interface structure is not clear at the moment. Nevertheless, at 573 K, oxygen release completed throughout the entire area of **Particle 2** (Fig. 2(d-2)).

In the case of **Particle 3** without Pt, oxygen storage proceeded independently of the absence of Pt, and oxygen diffusion from the CZ surface into the bulk was observed (Figs. 2(a-3) and 2(b-3)). The different modes of oxygen diffusion in **Particles 2** and **3** are thought to be caused by differences in the heterogeneous domain structures in the CZ particles. In contrast, oxygen release was almost inactive at 423 K (Fig. 2(c-3)) and was not completed at 573 K because blue parts still remained in Fig. 2(d-3). These results suggest that the absence of Pt strongly affected the reaction rate of oxygen release, in agreement with the results of TPR. Nano-XANES spectra of **Particles 1** and **3** agreed with the results of the 2D mapping of the Ce oxidation states (Figs. S9 and S10). Similar trends were observed for other particles (Fig. S11).

Oxygen diffusion is the key process of oxygen storage/release function and proceeds by changing the Ce oxidation states in CZ. In the oxygen storage process, the activation of O_2 is thought to proceed at defect sites on the surface of the pyrochlore structure parts of the CZ support and the subsequent oxygen diffusion spreads into the CZ bulk. The nano-XAFS imaging visualized the heterogeneous domains forming in the oxygen diffusion process even in the CZ crystal particles with single-phase XRD pattern. The heterogeneous domains are thought to provide a different distribution of surface defect sites, resulting in the heterogeneous reaction in individual particles observed in Fig. 2(a).

In contrast, oxygen release by reduction with H_2 initiates at the Pt catalysts on the surface of κ-phase CZ. *In situ* time-resolved XAFS analysis of Pt/CZ revealed the activation energy of oxygen release as 43 kJ mol^{-1} at both the Ce L_{III}- and Zr *K*-edges.[5] The reaction mechanism of oxygen release on Pt/ceria has been discussed, and it was reported that morphology of ceria support was highly affected to oxygen transfer on nanostructured ceria in close contact with Pt.[13] If activated hydrogen formed on the Pt catalyst transfers by spillover to the entire surface of CZ, color changes in the mapping of Ce oxidation states in Fig. 2(c-2) would be independent to the position of Pt. The anisotropic results in Fig. 2(c-2) imply that activated hydrogen formed on the Pt catalyst reacts with oxygen at the interface of Pt and κ-phase CZ and oxygen diffusion proceeds inside the CZ particle to the interface. The CZ support itself does not smoothly promote the reduction process, resulting in incomplete oxygen release in the CZ bulk observed in Figs. 2(c/d-3).

Practical three-way conversion catalysts consist of nanosized Pt particles on the surface of a Ce-based support. Although the support material intrinsically has structural heterogeneity, it is thought that nano-sized Pt catalysts spread on the support surface could make up for the heterogeneous reactivity of each domain structure in the support. The nano-XAFS imaging succeeded in visualizing and identifying the modes of heterogeneous reaction and active parts in individual catalyst particles for the oxygen storage/release in solid-solution for the first time, which may be promising for providing a new insight into deeper understanding of heterogeneous catalysis and developing new practical catalyst systems.

Experimental Section

Sample preparation: Pt (7.7 mg; Alfa Aesar) was impregnated with CZ (66.4 mg) in 2 mL of CH_3CN, and the solvent was evaporated. The obtained sample (3 mg) was added to 10 mL of ethanol and mixed by ultrasonic treatment for 30 min. 4 μL of the suspension was dropped onto a SiN membrane (NTT-AT; 2 mm × 2 mm × 100 nm) with Pt grids (5 μm width, 100 μm interval) and the membrane was dried in air. The process was repeated 10 times, and the obtained membrane was calcined at 573 K for 30 min. The oxygen storage/release reactions of the membrane were performed in a XAFS cell with flow of O_2 or 10% H_2/N_2 in 1000 mL min^{-1}. The details of the experiments are presented in Supporting information 11.

Characterization: The dispersion of sample particles on the SiN membrane was characterized by SEM analysis (JEOL JSM-6701F field emission SEM with BEI mode, 5.0 kV). XRD (Rigaku MultiFlex-STe, Cu *K*α, 40 kV, 50 mA) was measured under air, and the (440) diffraction peak (2θ = 47.7–48.8°) was used for the attribution of CZ phases.

Scanning nano-XRF and nano-XAFS were measured at the BL36XU and BL39XU beamlines at SPring-8, Japan. X-rays from an undulator were monochromatized by Si(111) crystals and focused by Kirkpatrick-Baez mirrors to a size of 409 (h)×154 (v) nm (6 keV). The sample enclosed in the XAFS cell with He flow was mounted on an encoded-feedback translation stage (10 nm resolution) at the focal point of the X-ray beam, inclined at a tilt of 30° to the optical path. Incident and fluorescent X-rays were detected by a He-filled ion chamber and a 21-element Ge detector (Canberra, EGPX 40×40×7-21PIX), respectively. Scanning nano-XRF mappings were measured every 150 nm at the 122 energies around the Ce L_{III}-edge (5.68-5.80 keV). In addition to Ce *L*α

fluorescent X-rays, Pt *L*α florescent X-rays were also detected by using higher-order light. Analysis of the obtained imaging data was performed by the reported method.[9] Oxygen composition was estimated by linear combination fitting of the Ce L_{III}-edge nano-XANES spectra of pyrochlore $Ce_2Zr_2O_7$ and κ-phase $Ce_2Zr_2O_8$.

Keywords: Heterogeneous catalysis • ceria-zirconia • oxygen storage capacity • XAFS imaging • structure-activity relationships

[1] S. Mitchell, NL. Michels, J. Pérez-Ramírez, *Chem. Soc. Rev.* **2013**, *42*, 6094.

[2] a) H. C. Yao, Y. F. Yu Yao, *J. Catal.* **1984**, *86*, 254; b) J. Kašpar, P. Fornasiero, M. Graziani, *Catal. Today* **1999**, *50*, 285; c) S. Matsumoto, *Catal. Today* **2004**, *90*, 183.

[3] A. Suda, Y. Ukyo, H. Sobukawa, M. Sugiura, *J. Ceram. Soc. Jpn*. **2002**, *110*, 126.

[4] a) T. Tanabe, A. Suda, C. Descorme, D. Duprez, H. Shinjoh, M. Sugiura, *Stud. Surf. Sci. Catal*. **2001**, *138*, 135; b) P. Fornasiero, J. Kašpar, V. Sergo, M. Graziani, *J. Catal*. **1999**, *182*, 56.

[5] T. Yamamoto, A. Suzuki, Y. Nagai, T. Tanabe, F. Dong, Y. Inada, M. Nomura, M. Tada, Y. Iwasawa, *Angew. Chem., Int. Ed.* **2007**, *46*, 9253.

[6] a) M. Tada, S. Zhang, S. Malwadkar, N. Ishiguro, J. Soga, Y. Nagai, K. Tezuka, H. Imoto, S. O.-Y.-Matsuo, S. Ohkoshi, Y. Iwasawa, *Angew. Chem. Int. Ed.* **2012**, *51*, 9361; b) M. Tada, N. Ishiguro, T. Uruga, H. Tanida, Y. Terada, S. Nagamatsu, Y. Iwasawa, S. Ohkoshi, *Phys. Chem. Chem. Phys.* **2011**, *13*, 14910.

[7] a) I. L. C. Buurmans, B. M. Weckhuysen, *Nature Chem*. **2012**, *4*, 873; b) B. M. Weckhuysen, *Angew. Chem. Int. Ed.* **2009**, *48*, 4910.

[8] a) S. Kalirai, U. Boesenberg, G. Falkenberg, F. Meirer, B. M. Weckhuysen, *ChemCatChem* **2015**, *7*, 3674; b) F. Meirer, D. T. Morris, S. Kalirai, Y. Liu, J. C. Andrews, B. M. Weckhuysen, *J. Am. Chem. Soc.* **2015**, *137*, 102; c) S. Takao, O. Sekizawa, S. Nagamatsu, T. Kaneko, T. Yamamoto, G. Samjeské, K. Higashi, K. Nagasawa, T. Tsuji, M. Suzuki, N. Kawamura, M. Mizumaki, T. Uruga, Y. Iwasawa, *Angew. Chem. Int. Ed.* **2014**, *53*, 14110; d) T. Saida, O. Sekizawa, N. Ishiguro, M. Hoshino, K. Uesugi, T. Uruga, S. Ohkoshi, T. Yokoyama, M. Tada, *Angew. Chem. Int. Ed.* **2012**, *124*, 10457; e) I. D. Gonzalez-Jimenez, K. Cats, T. Davidian, M. Ruitenbeek, F. Meirer, Y. Liu, J. Nelson, J. C. Andrews, P. Pianetta, F. M. F. de Groot, B. M. Weckhuysen, *Angew. Chem. Int. Ed.* **2012**, *51*, 11986.

[9] N. Ishiguro, T. Uruga, O. Sekizawa, T. Tsuji, M. Suzuki, N. Kawamura, M. Mizumaki, K. Nitta, T. Yokoyama, M. Tada, *ChemPhysChem* **2014**, *15*, 1563.

[10] P. Fornasiero, G. Balducci, R. Di Monte, J. Kašpar, V. Sergo, G. Gubitosa, A. Ferrero, M. Graziani, *J. Catal.* **1996**, *164*, 173.

[11] T. Omata, H. Kishimoto, S. Otsuka-Yao-Matsuo, N. Ohtori, N. Umesaki, *J. Solid State Chem.* **1999**, *147*, 573.

[12] a) J. El Fallah, S. Boujana, H. Dexpert, A. Kiennemann, J. Majerus, O. Touret, F. Villain, F. Le Normand, *J. Phys. Chem.* **1994**, *98*, 5522; b) D. R. Modeshia, C. S. Wright, J. L. Payne, G. Sankar, S. G. Fiddy, R. I. Walton, *J. Phys. Chem. C* **2007**, *111*, 14035.

[13] G. N. Vayssilov, Y. Lykhach, A. Migani, T. Staudt, G. P. Petrova, N. Tsud, T. Skála, A. Briux, F. Illas, K. C. Prince, V. Matolin, K. M. Neyman, J. Libuda, *Nature Mat.* **2011**, *10,* 310.

Entry for the Table of Contents

Layout 1:

COMMUNICATION

Visualizing heterogeneous reaction mode: Oxygen diffusion in individual Pt/$Ce_2Zr_2O_x$ particles in a three-way conversion catalyst was imaged by scanning nano-XAFS. Heterogeneous oxygen diffusion modes and active parts were successfully visualized for oxygen storage/release.

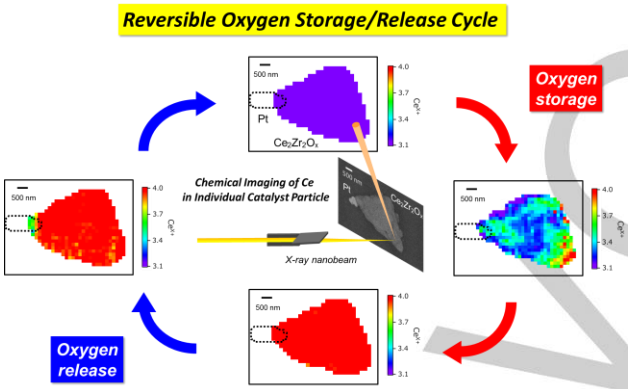

Dr. Hirosuke Matsui, Dr. Nozomu Ishiguro, Kaori Enomoto, Dr. Oki Sekizawa, Prof. Dr. Tomoya Uruga, and Prof. Dr. Mizuki Tada

Page No. – Page No.

Imaging of Oxygen Diffusion in Individual Pt/$Ce_2Zr_2O_x$ Catalyst Particles for Oxygen Storage/Release Cycle